



Universidad Autónoma
de Madrid

Biblos-e Archivo
Repositorio Institucional UAM

Repositorio Institucional de la Universidad Autónoma de Madrid

<https://repositorio.uam.es>

Esta es la **versión de autor** del artículo publicado en:
This is an **author produced version** of a paper published in:

Journal of Biophotonics 13.11 (2020): e202000154

DOI: <https://doi.org/10.1002/jbio.202000154>

Copyright: © 2020 Wiley-VCH

El acceso a la versión del editor puede requerir la suscripción del recurso

Access to the published version may require subscription

This paper must be cited as:

Lifante J, del Rosal B, Chaves-Coira I, Fernández N, Jaque D, Ximendes E.
The near-infrared autofluorescence fingerprint of the brain. *J. Biophotonics*. 2020; e202000154

The near-infrared autofluorescence fingerprint of the brain.

José Lifante,^{1,2} Blanca del Rosal,³ Irene Chaves-Coira,⁴ Nuria Fernández,^{1,2} Daniel Jaque^{1,2*} and Erving Ximendes.^{1,2}

¹ Fluorescence Imaging Group, Universidad Autonoma de Madrid, Madrid 28049, Spain.

² Nanobiology Group, Instituto Ramón y Cajal de Investigación Sanitaria, IRYCIS Madrid, Spain

³ Centre for Micro-Photonics, Faculty of Science, Engineering and Technology, Swinburne University of Technology, Hawthorn, VIC, 3122 Australia.

⁴ Department of Anatomy, Histology and Neuroscience, Faculty of Medicine, Universidad Autónoma de Madrid, 28049 Madrid, Spain

E-mail: daniel.jaque@uam.es

This document is the unedited Author's version of a Submitted Work that was subsequently accepted for publication in *Journal of Biophotonics*, copyright © 2020 Wiley-VCH GmbH after peer review. To access the final edited and published work see:

<https://onlinelibrary.wiley.com/doi/full/10.1002/jbio.202000154>

Abstract

The brain is a vitally important organ involved in most of the central nervous system disorders. Their diagnosis and treatment require technologies capable of fast, cost-effective, high-resolution and high-sensitivity imaging. The combination of a new generation of luminescent nanoparticles and fluorescence imaging systems working in the second biological near-infrared window (NIR-II) is emerging as a reliable alternative over conventional brain imaging techniques. For NIR-II imaging to become a robust imaging technique at the preclinical level, a full knowledge of the NIR-II brain autofluorescence, responsible for the loss of image resolution and contrast is required. In this work, we demonstrate that the brain shows a peculiar infrared autofluorescence spectrum that can be explained in terms of specific molecular components including neuromelanin and lipids. We also provide experimental evidence of the existence of particular structures within the brain with well-defined near-infrared autofluorescence fingerprints, opening the door to *in vivo* anatomical imaging *via* near-infrared fluorescence analysis. Finally, we propose a rational selection of infrared luminescent probes for brain imaging based on their spectral overlap with brain autofluorescence.

Significance Statement

Using state-of-the-art NIR-II hyperspectral imaging, we have assessed the autofluorescence of the brain in the near-infrared, characterized its spectral features and ascertained its origin. The dominant presence of lipids, myelin and neuromelanin in the brain is the root cause of its particular autofluorescence fingerprint. This characterization enables a rational selection of NIR-II fluorophores for high-contrast, high-resolution brain imaging as autofluorescence cannot be neglected when performing transcranial imaging with available NIR-II contrast agents. Further, the non-homogeneous distribution of the autofluorescence of the brain opens up the possibility of autofluorescence-based imaging of brain structures, removing the need for contrast agents. This, in turn, could enable developing novel, minimally invasive diagnostic procedures based on changes in brain autofluorescence.

Fast and cost-effective brain imaging is nowadays possible by using fluorescent contrast agents working in the second near-infrared region (NIR-II). Exploitation of this technology requires full knowledge of the NIR-II autofluorescence of brain as its presence has a negative impact on the contrast and resolution of acquired images. Whole body hyperspectral imaging is used to assess the *in vivo* brain autofluorescence. *In vivo* and *ex vivo* experiments demonstrate that brain possesses an infrared autofluorescence fingerprint consequence of its unique composition. Furthermore, brain autofluorescence has been found to show a high spatial inhomogeneity, opening the door to anatomical brain imaging without requiring the use of NIR-II contrast agents.

Introduction

Central nervous system (CNS) disorders currently affect close to 2 billion people worldwide. This figure is expected to increase due to the progressive ageing of the population, as the prevalence of these diseases increases steeply with age. CNS disorders are the leading cause of disability worldwide, imposing a large burden on healthcare systems (1). Most of them are likely associated with subtle neuropathological changes, which are virtually undetectable until they reach a certain threshold of tissue damage (2). Thus, being able to detect the very first pathological hallmarks of disease would allow developing new therapeutic strategies aimed to minimize the impact of CNS disorders. Several clinical imaging modalities such as single-photon emission computed tomography (SPECT), positron emission tomography (PET), magnetic resonance imaging (MRI) or ultrasound imaging enable anatomical and functional imaging of the central nervous system. However, these techniques have some major drawbacks including the use of ionizing radiation (SPECT, PET), low acquisition speeds and high costs (MRI) and low spatial resolutions (ultrasound). Thus, implementing novel non-invasive, cost-effective, non-ionizing techniques with a high spatial and temporal resolution for *in vivo* brain imaging would constitute a major breakthrough (3).

Near-infrared (NIR) fluorescence imaging could overcome the intrinsic limitations of conventional imaging modalities. It relies on the partial transparency of biological tissues to NIR radiation to achieve high-contrast, deep-tissue imaging (4, 5). Recently, NIR-emitting organic molecules and nanoparticles (NPs) have been used for transcranial fluorescence brain imaging. As a consequence, non-invasive *in vivo* imaging of the brain vasculature, brain tumour detection, and image-assisted surgery have been achieved (6). Other applications, such as *in vivo* mesenchymal stem cell tracking or intracranial nanothermometry have also been demonstrated (7, 8).

Despite the recent progress on NIR-II brain imaging (see **SI Appendix, Table S1**), this technique is still in its early stages and some key potential pitfalls remain unexplored. One of them is the possible interference of NIR-II brain autofluorescence that can hinder the contrast and resolution of NIR-II *in vivo* fluorescence images. Yet, this brain autofluorescence has been systematically disregarded (9, 10). As part of the development of NIR-II fluorescence imaging for preclinical applications, researchers have focused on developing strategies for autofluorescence background removal (11). While the combination of long-lifetime NIR-II probes with time-gated image acquisition allows autofluorescence-free imaging (12-14), this approach is unsuitable for transcranial imaging due to the reduced fluorescence lifetimes ($<1\ \mu\text{s}$) of most of the available NIR-II probes (15). Alternatively, autofluorescence-free imaging is possible using contrast agents emitting well into the NIR-II, as autofluorescence intensity decreases at longer wavelengths. The combination of these probes with spectral filters then becomes a cost-effective and reliable approach for whole-body autofluorescence-free *in vivo* imaging (9). This approach calls for a rational selection of the NIR-II luminescence probes to minimize the spectral overlap between their emission and the tissue autofluorescence. This, in turn, requires a full knowledge of the NIR-II autofluorescence of the tissues under study.

Fully characterizing NIR-II brain autofluorescence could not only allow for autofluorescence-free imaging, but it might also contribute to developing new diagnostic strategies. Tissue autofluorescence depends on the concentration and spatial distribution of endogenous fluorophores, so its corresponding spectrum contains information about the molecular composition of that tissue (16). Histological and histochemical changes associated with disease development could then be tracked by changes in the autofluorescence. This has already been demonstrated for the diagnosis of unstable atheroma plaques (17). In the case of the brain, observable changes in its characteristic autofluorescence could be useful indicators of CNS disorders. For instance, brain has a high content of myelin that is a known source of autofluorescence in the visible spectral range and increases during neuronal aging and in the development of some neurodegenerative disorders (18-21).

Despite its relevance for high contrast, fast and cost-effective imaging, the NIR-II brain autofluorescence remains unexplored. In this work, we report for the first time on the *in vivo* NIR-II autofluorescence of the mouse brain as obtained by hyperspectral imaging under optical excitation at 808 nm. We have systematically compared the *ex-vivo* NIR-II autofluorescence of the brain to that of other organs and explained the observed differences considering the particular composition of the brain. We have spatially mapped the NIR-II autofluorescence of the brain and observed a non-homogeneous signal that has been correlated with the presence of well-defined structures rich in neuromelanin (NM), thus identifying the first specific NIR-II endogenous brain fluorophore. We discuss potential future applications of NIR-II autofluorescence in the context of specific CNS disorders, such as melanoma and Parkinson. Finally, we have analyzed the spectral overlap between the autofluorescence of the brain and the emission bands of NIR-II fluorescence probes used for transcranial imaging to identify the most suitable probes for autofluorescence-free NIR-II brain imaging.

Results and discussion

NIR-II hyperspectral characterization of brain autofluorescence

Hyperspectral Imaging (HIS) in the NIR-II, as described in **SI Appendix, Section S2** allows for the acquisition of the *in vivo* infrared autofluorescence spectra at submillimeter spatial resolution. This, in turn, allows identifying differences between the autofluorescence spectra generated by different tissues and/or their substructures. To compare the *in vivo* autofluorescence of the brain to that of other organs, we performed HIS on a C75Bl6/J mouse under illumination at 808 nm. A part of the skull on the left cerebral hemisphere had been removed prior to the experiment to expose the brain cortex (**Fig. 1A**). The narrowband autofluorescence images from the abdominal (**Fig. 1B**) and cerebral (**Fig. 1C**) regions were recorded in the 900-1600 nm wavelength range and the spectra corresponding to both regions were obtained (**Fig. 1D**). As observed in **Fig. 1C**, the site where the cranial window was created presented a lower emission intensity than the regions covered by the skull. Though seemingly counter-intuitive, such results are expected in light of the transmission and autofluorescence properties of skull (**SI Appendix, Section S3**). In reasonable agreement with previously published data (10), the autofluorescence spectrum of the abdominal region was characterized by long tail extending up to 1100 nm. The autofluorescence spectrum shows a peak centered at around 1015 nm that is superimposed to the long tail (10). The *in vivo* autofluorescence of the brain, on the other hand, presented different spectral features including an extra peak centered at 1075 nm that is not present in the abdominal autofluorescence spectrum.

To understand the origin of the peculiar NIR-II autofluorescence of the brain and to rule out the presence of artefacts in the hyperspectral measurements, we recorded the autofluorescence spectrum of different *ex-vivo* organs under the same experimental conditions. **Fig. 2A** shows an optical image of the different organs harvested from a healthy C57BL/6J mouse. The narrowband fluorescence images obtained from these organs at different wavelengths are also shown in **Fig. 2A**. A detailed analysis of these monochromatic images reveals that the wavelength dependence

of the autofluorescence differs from organ to organ. The autofluorescence spectra reconstructed from them allows splitting the analyzed tissues into three groups:

- i) **Type I.-** Tissues showing a NIR-II autofluorescence spectrum constituted by a broad fluorescence tail (**Fig. 2B**).
- ii) **Type II.-** Tissues with a NIR-II autofluorescence spectrum constituted by a single peak at 1015 nm superimposed to the broad fluorescence tail (**Fig. 2C**).
- iii) **Type III.-** Tissues showing a NIR-II autofluorescence spectrum constituted by two peaks at 1015 nm and 1075 nm superimposed to the broad fluorescence tail (**Fig. 2D**).

All analyzed tissues, except for the brain, fall into either Type I or Type II groups. In this sense, the brain shows a peculiar autofluorescence. Type I tissues show a NIR-II autofluorescence spectrum similar to that of the liver (which is in good agreement with previously reported data (22), as it is evidenced in **SI Appendix, Section S4**. On the other hand, the adipose tissue could be selected as a representative example within Type II group. The fact that the adipose tissue shows the largest contribution of the 1015 nm peak to the overall autofluorescence spectrum seems to indicate that this particular peak arises from the presence of lipids. This would explain why this peak is also present in the brain autofluorescence spectrum, as the brain is rich in lipids (20). The contribution of the autofluorescence peak at 1075 nm, on the other hand, should be ascribed to a fluorophore that is specifically enriched in the brain. Independently of the fluorophore responsible for the spectral features of the autofluorescence, a proper analysis of autofluorescence images could be useful for anatomical imaging as it is the only tissue showing this 1075 nm emission line. A ratiometric analysis of the hyperspectral autofluorescence allows clearly differentiating the brain from other tissues as shown in **SI Appendix, Section S5**.

Imaging the heterogeneous composition of brain by NIR-II autofluorescence

To obtain further information about the origin of the peculiar NIR-II brain autofluorescence, a series of high magnification *ex vivo* autofluorescence images of a brain from a C57BL/6J mouse were recorded at different wavelengths. The obtained results, together with an optical image of the brain under study, are shown in **Fig. 3A**. As described previously, the autofluorescence of the brain decreases with increasing wavelength – with intensity maxima at around 1015 and 1075 nm. On top of this general observation, a detailed inspection of the autofluorescence images reveals a non-homogeneous spatial behavior. In particular, the narrowband autofluorescence image at 1150 nm reveals that the signal is only generated from a very well localized area (indicated by a blue square in both optical and fluorescence image) whereas the rest of the brain shows no autofluorescence at this wavelength. Direct visual inspection reveals the presence of a well-demarcated black area (see green squares in the optical image of **Fig. 3A**) that coincides with the anatomical location and shape of the fluorescence image in the 1100–1300 nm wavelength range (**SI Appendix, Section S6**). According to previous studies C57BL/6J mouse brain (22, 23), such structures can be identified as melanosomes found between the olfactory bulbs and cerebral hemispheres. Hence, as these vesicles are enriched with a dark-neural pigment known as neuromelanin (NM), we can suggest that this characteristic autofluorescence is caused by the presence of neuromelanin (NM). (24). The differences between the autofluorescence spectra of the right cortex and of the frontal brain (exposed after olfactory bulb resection as indicated by the letters A and B in **Fig. 3A**) are further evidenced in **Fig. 3B**. Though the peaks at 1015 and 1075 nm are present in both cases, the rostral brain shows a larger contribution in the 1100-1300 nm range.

Results of **Fig. 3** reveal the capability of autofluorescence imaging for identifying different structures inside the brain. In particular, NIR-II brain autofluorescence emerges as a straightforward technique for the localization and monitoring of the local content of NM. This is of particular importance for clinical applications. As a matter of fact, NM is a brain pigment naturally expressed in melanocytes, a cell type that have been recently described to comprise a population capable of myelinate the axons of mouse neurons (24). Melanosomes are originated by accumulation of the NM pigment in autophagic phagosomes inside the cells which are enriched in lipids such as dolichols and dolichols

acids (25). Unlike non-neural melanins such as those present in the skin, the melanosomes in the brain are not synthesized under a controlled enzymatic pathway. Instead, they are spontaneously generated after free-radical oxidation of dopamine, norepinephrine and other catecholamines to semi-quinones and quinones in the cytosol of the neuronal cells (26). Differentially to mouse brain, in humans NM is strongly expressed in noradrenergic neurons of the *substantia nigra pars compacta* and *locus coeruleus*, leading to a black appearance in these regions of aged brains. Loss of NM and subsequent depigmentation of these brain regions is a hallmark feature of Parkinson disease (PD) (27). Importantly, PD diagnosis occurs when motor symptoms are already apparent and 30% or more of the *substantia nigra* dopamine neurons are already dead revealing the importance of the development of early diagnosis techniques. Neuromelanin detection by MRI has recently been proposed as a promising biomarker for Parkinson disease (28) and this work opens the way towards early cost effective and fast early diagnosis of Parkinson through the analysis of NIR-II brain autofluorescence.

Further, an early detection of an increase of neuromelanin in the brain could be relevant in other scenarios, such as in the diagnosis of brain melanomas. Metastases to the brain are observed in 10–40% of primary cutaneous melanoma patients, with a detection time between 1 and 5 years and an extremely poor prognosis, with a median overall survival of 4–5 months after diagnosis (29).

Rational selection of NIR-II nanoprobes for *in vivo* transcranial imaging

As already mentioned, NIR-II autofluorescence could have a negative impact on the contrast of brain images when NIR-II fluorescence probes are used as contrast agents. Minimum overlap between the emission of these NIR-II probes and brain autofluorescence spectra is then desired as it would enable the effective removal of autofluorescence background by straightforward spectral filtering. The knowledge of the NIR-II autofluorescence of the brain allows evaluating the suitability of the different NIR-II probes for high contrast brain imaging. To quantify the overlap between the emission of NIR-II probes and the autofluorescence of the brain, we have used the dimensionless overlap parameter Γ , defined as:

$$\Gamma = \frac{[\int I_{Brain} \cdot I_{NP} \cdot d\lambda]^2}{[\int I_{Brain}^2 \cdot d\lambda] \cdot [\int I_{NP}^2 \cdot d\lambda]} \quad (1)$$

where I_{Brain} and I_{NP} are the emission intensity from the brain and the NIR-II fluorescent probe, respectively. The integrals extend along the full spectral range of the emissions. Under such a definition, the overlap parameter Γ can range from 0 (no overlap, ideal case for background-free brain imaging) to 1 (equal shape of the two emission bands leading to poor contrast in brain imaging). **Fig. 4** shows the brain autofluorescence together with the emission of the most widely used contrast agents in NIR-II imaging – organic dyes (**Fig. 4A**), rare-earth-doped nanoparticles (**Fig. 4B**), quantum dots (**Fig. 4C**), and single-walled carbon nanotubes (**Fig. 4D**). The spectral overlap factor Γ between the emission of each probe and the autofluorescence of the brain is also shown. As can be observed, Γ ranges from high to moderate (**Fig. 4A and 4D**) to low or negligible (**Fig. 4B and 4C**). All NIR-II contrast agents evaluated here show non-negligible spectral overlaps with the autofluorescence of the brain except for erbium-doped nanoparticles, which show an emission band at around 1500 nm that makes them ideal for autofluorescence-free NIR-II brain imaging. Other widely used probes, such as Ag₂S nanoparticles, show a relevant overlap with autofluorescence that has so far been neglected. This fact indicates that brain images obtained using these NIR-II contrast agents contain, very likely, some background contribution from autofluorescence. Image contrast and spatial resolution could be easily improved in this case by using of bandpass or long pass filters.

Conclusions

In summary, we have applied state of the art in NIR-II imaging technology (whole body hyperspectral infrared imaging) to assess the *in vivo* infrared autofluorescence of the brain. We found that, when compared to other organs, the brain presents a peculiar infrared autofluorescence that can be attributed to its unique composition. In particular, we state that the dominant presence of lipids, melanin and neuromelanin in the brain is what causes its distinct autofluorescence fingerprint. The detailed characterization of the NIR brain autofluorescence provided here allows for the rational selection of NIR-II luminescent probes towards high contrast and high-resolution brain imaging. We have also demonstrated how the presence of autofluorescence images obtained with widely used NIR-II contrast agents (such as carbon nanotubes or Ag₂S nanoparticles) cannot be neglected, leading to a deterioration in image background and contrast. Finally, we have also provided experimental evidence of the non-homogeneous distribution of brain autofluorescence, revealing the possibility of imaging brain structures based on their autofluorescence – that is, removing the need for contrast agents.

Materials and Methods

Hyperspectral imaging

The hyperspectral imaging setup used for the acquisition of the NIR-II autofluorescence spectra of brain and other tissues is schematically represented in the **SI Appendix, Figure S1**. The freshly dissected tissue was optically excited with an 808 nm fiber-coupled laser diode (LIMO). A short-pass filter (Thorlabs FES0850) was placed immediately in front of the laser fiber to minimize specular and diffuse reflection effects. The illumination intensity was controlled by adjusting the fiber-to-tissue distance. In all the experiments its value was fixed at 50 mW/cm². This intensity prevented excessive tissue heating and subsequent drying. The autofluorescence plus 808 nm scattered light generated by the tissue was spectrally filtered with two consecutive long-pass filters (Thorlabs FEL0850) that were used to block the 808 nm back-scattered signal and isolate the autofluorescence. A combination of shortwave infrared (SWIR) lenses were used to send the autofluorescence signal on to a Bragg tunable filter, which allows to select a specific wavelength of the incoming light. A second tube lens focuses after the filtered light on a near-infrared camera (ZephIR™ 1.7) to produce a monochromatic image. To cover a specific spectral range, each monochromatic image was recorded and then stored on a computer while the angle of the BTF rotation stage was continuously tuned. At the end of this process, the system built up a Hyperspectral (HIS) cube, i.e. a 3D spatial map of spectral variation: the first two dimensions providing spatial information and a third dimension accounting for the spectral information. The intensity values of a particular pixel in a HIS cube characterize its unique spectral fingerprint.

In vivo NIR-II autofluorescence imaging

For this study, one C57BL/6J male mouse (20-22 weeks old) was used. Deep anesthesia was induced with 4.6% of inhaled isoflurane under a constant flow rate of 0.5 mL/min, and maintained between 2.5 – 3.0 % during the surgical procedure to perform a cranial window to expose the left cerebral cortex.

Briefly, the anesthetized mouse was placed in a stereotaxic frame. The scalp was cut so the skull was clearly exposed. Posterior craniotomy was performed using a dremmel so an ipsilateral window was open to expose the left hemisphere of the brain. The anesthetized animal was then

placed into the experimental hyperspectral imaging chamber to collect the autofluorescence images as described above.

Ex vivo fluorescence imaging

For this study a total of 3 C57BL/6J male mice (20-22 weeks old) were used. Animals were euthanized by beheading after induction of deep anesthesia with isoflurane under a constant O₂ flow rate of 0.5 mL/min and a concentration of 4.6% of isoflurane. The organs were immediately removed and washed thoroughly with cold 0.9% NaCl solution prior to fluorescence imaging in order to slow down their degradation. The time between sacrifice and imaging was shorter than five minutes for all experiments. Hyperspectral images of brain tissue autofluorescence under an 808 nm continuous wave laser excitation were obtained with a spectral resolution of 5 nm and an exposure time of 20 seconds. The intensity of the laser was fixed at 50 mW/cm².

Animal experiments

Procedures involving animal experiments were approved by the regional authority for animal experimentation of Comunidad de Madrid and were conducted in agreement with the Universidad Autónoma de Madrid Ethics Committee, in compliance with the European Union directives 63/2010UE and Spanish regulation RD 53/2013.

Acknowledgments

This work was supported by the Spanish Ministry of Economy and Competitiveness under projects MAT2016-75362-C3-1-R, MAT2017-83111R, and MAT2017-85617-R, by the Instituto de Salud Carlos III (PI16/00812), by the Comunidad Autónoma de Madrid (B2017/BMD-3867RENIMCM), and co-financed by the European Structural and investment fund. Additional funding was provided by the European Commission, Horizon 2020 project NanoTBTech (801305), the Fundación para la Investigación Biomédica del Hospital Universitario Ramón y Cajal project IMP18_38 (2018/0265) and also by COST action CA17140. Y.L.S. acknowledges a scholarship from the China Scholarship Council (No. 201806870023).

Author Contributions

Jose Lifante and Erving Ximendes contributed to the imaging experiments and the writing of this manuscript. Irene Chaves-Coira contributed to the design and development of *in vivo* experiments. Nuria Fernandez, Blanca del Rosal and Daniel Jaque contributed to the design of the experiments, data analysis and the writing of this manuscript.

Figures and Tables

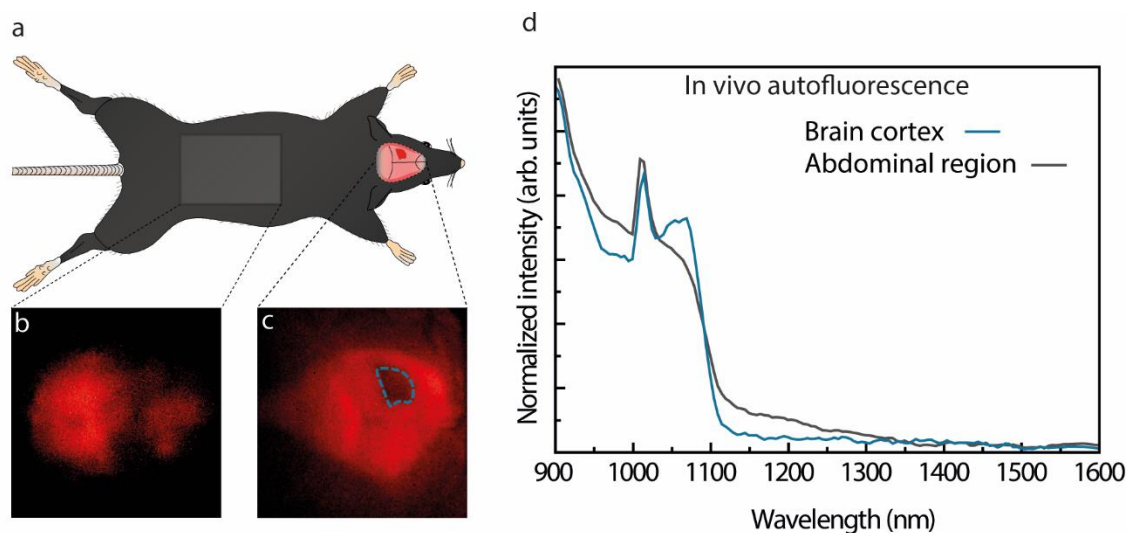


Fig 1: Comparative *in vivo* autofluorescence of the brain and the abdominal organs in a C57BL/6J mouse. **(a)** Representative image of a typical C57BL/6J in which the skull of the left cerebral hemisphere of the brain has been removed to expose the brain. *In vivo* narrowband brain autofluorescence images of **(b)** abdominal region and **(c)** cranial window under 808 nm excitation. **(d)** *In vivo* autofluorescence spectra of abdominal region and brain cortex.

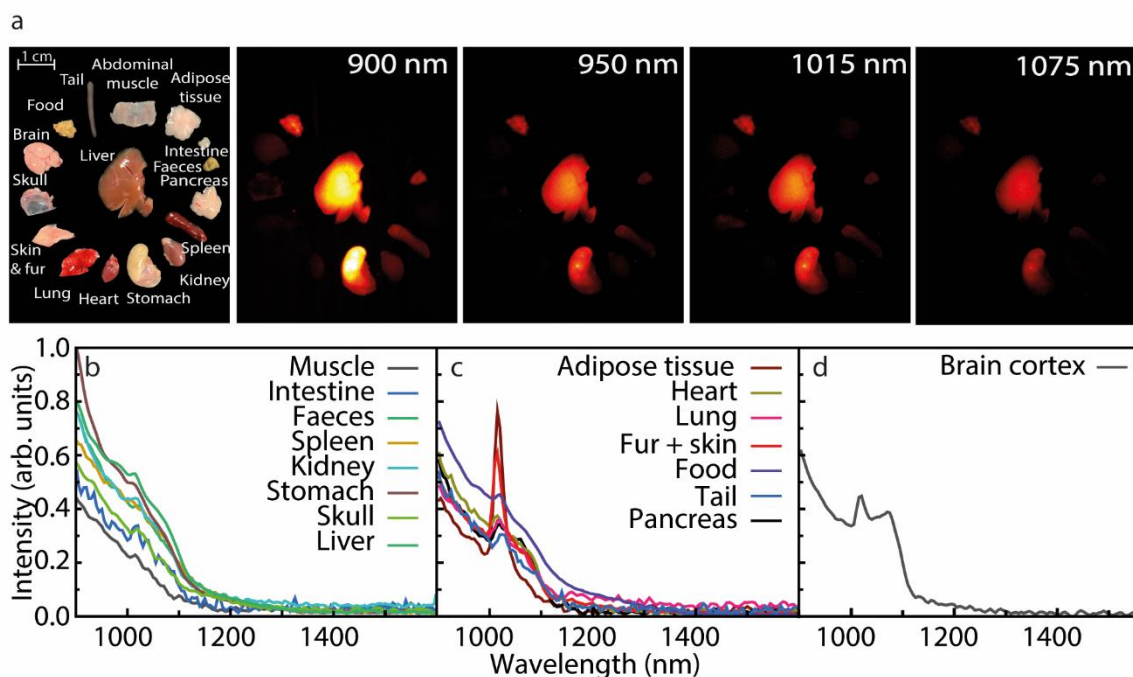


Fig 2: Autofluorescence images of major organs at selected wavelengths in the NIR-II window. **(a)** Optical and *ex vivo* autofluorescence images (centered at 900, 950, 1015 and 1075 nm), obtained under 808 nm excitation, of selected organs harvested from a C57BL/6J mouse. **(b)** Autofluorescence spectra of organs showing an autofluorescence tail (Type I), **(c)** an autofluorescence emission peak at 1015 nm (Type II) and **(d)** two autofluorescence peaks at 1015 nm and 1075 nm (Type III).

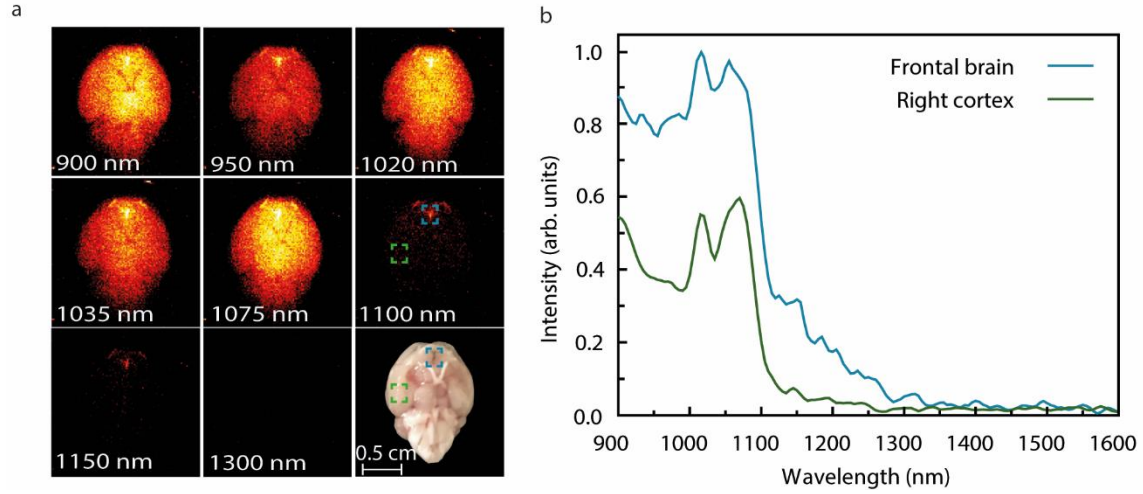


Fig 3: Spatial distribution of NIR-II brain autofluorescence. (a) Autofluorescence images of a C57BL6/J mouse under 808 nm continuous excitation at selected wavelengths. The optical image of the analyzed brain is also included. The squares in the right image in the middle row indicate the location of the frontal brain and the right cortex. **(b)** Autofluorescence spectra as obtained at the locations indicated by the squares in (a).

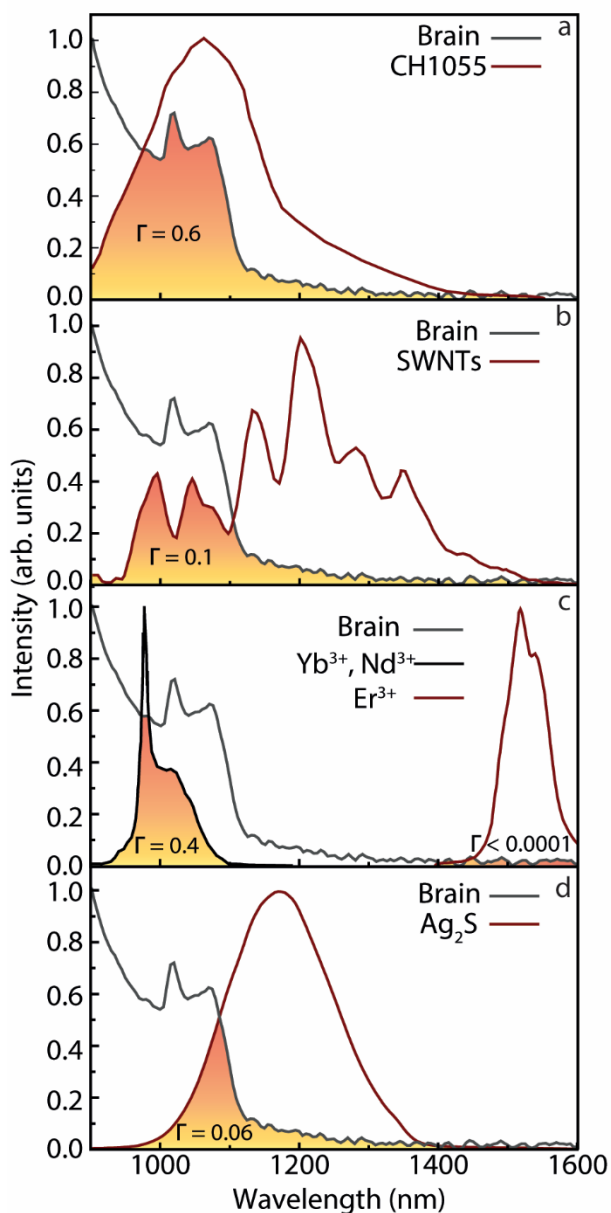


Fig 4: Overlap integral between brain autofluorescence and four selected nanoprobe used for brain imaging. (a) Brain autofluorescence spectral overlap with (a) CH1055 organic dye (30), (b) SWCNTs (31), (c) Rare-earth doped nanoparticles (32) and (d) Ag₂S nanoparticles (8).

References

1. V. L. Feigin *et al.*, Global, regional, and national burden of neurological disorders during 1990–2015: a systematic analysis for the Global Burden of Disease Study 2015. *The Lancet Neurology* **16**, 877-897 (2017).
2. M. Katsuno, K. Sahashi, Y. Iguchi, A. Hashizume, Preclinical progression of neurodegenerative diseases. *Nagoya J Med Sci* **80**, 289-298 (2018).
3. J. N. D. Kerr, W. Denk, Imaging in vivo: watching the brain in action. *Nature Reviews Neuroscience* **9**, 195-205 (2008).

4. E. Hemmer, A. Benayas, F. L  gar  , F. Vetrone, Exploiting the biological windows: current perspectives on fluorescent bioprobes emitting above 1000 nm. *Nanoscale Horizons* **1**, 168-184 (2016).
5. R. R. Anderson, J. A. Parrish, The Optics of Human Skin. *Journal of Investigative Dermatology* **77**, 13-19 (1981).
6. G. Hong, A. L. Antaris, H. Dai, Near-infrared fluorophores for biomedical imaging. *Nature Biomedical Engineering* **1**, 0010 (2017).
7. G. Chen *et al.*, Recent Advances in Tracking the Transplanted Stem Cells Using Near-Infrared Fluorescent Nanoprobes: Turning from the First to the Second Near-Infrared Window. *Advanced Healthcare Materials* **7**, 1800497 (2018).
8. B. del Rosal *et al.*, In Vivo Contactless Brain Nanothermometry. *Advanced Functional Materials* **28**, 1806088 (2018).
9. I. Villa *et al.*, 1.3 μm emitting SrF₂:Nd³⁺ nanoparticles for high contrast in vivo imaging in the second biological window. *Nano Research* **8**, 649-665 (2015).
10. B. del Rosal, I. Villa, D. Jaque, F. Sanz-Rodr  guez, In vivo autofluorescence in the biological windows: the role of pigmentation. *J. Biophotonics* **9**, 1059-1067 (2016).
11. B. del Rosal, A. Benayas, Strategies to Overcome Autofluorescence in Nanoprobe-Driven In Vivo Fluorescence Imaging. *Small Methods* **2**, 1800075 (2018).
12. B. del Rosal *et al.*, Overcoming Autofluorescence: Long-Lifetime Infrared Nanoparticles for Time-Gated In Vivo Imaging. *Advanced Materials* **28**, 10188-10193 (2016).
13. X. Zheng *et al.*, High-Contrast Visualization of Upconversion Luminescence in Mice Using Time-Gating Approach. *Analytical Chemistry* **88**, 3449-3454 (2016).
14. M. Tan *et al.*, Rare-earth-doped fluoride nanoparticles with engineered long luminescence lifetime for time-gated in vivo optical imaging in the second biological window. *Nanoscale* **10**, 17771-17780 (2018).
15. C. Bouzigues, T. Gacoin, A. Alexandrou, Biological Applications of Rare-Earth Based Nanoparticles. *ACS Nano* **5**, 8488-8505 (2011).
16. M. Monici, "Cell and tissue autofluorescence research and diagnostic applications" in *Biotechnology Annual Review*. (Elsevier, 2005), vol. 11, pp. 227-256.
17. N. M. Htun *et al.*, Near-infrared autofluorescence induced by intraplaque hemorrhage and heme degradation as marker for high-risk atherosclerotic plaques. *Nat Commun* **8**, 75-75 (2017).
18. G. Gopalakrishnan *et al.*, Lipidome and proteome map of myelin membranes. *Journal of Neuroscience Research* **91**, 321-334 (2013).
19. A. Ishii *et al.*, Human myelin proteome and comparative analysis with mouse myelin. *Proceedings of the National Academy of Sciences* **106**, 14605 (2009).
20. K. Bozek *et al.*, Organization and Evolution of Brain Lipidome Revealed by Large-Scale Analysis of Human, Chimpanzee, Macaque, and Mouse Tissues. *Neuron* **85**, 695-702 (2015).
21. S. S. Seehafer, D. A. Pearce, You say lipofuscin, we say ceroid: Defining autofluorescent storage material. *Neurobiology of Aging* **27**, 576-588 (2006).
22. H. Barden, S. Levine, Histochemical observations on rodent brain melanin. *Brain Research Bulletin* **10**, 847-851 (1983).
23. S. A. H. Gudjohnsen *et al.*, Meningeal Melanocytes in the Mouse: Distribution and Dependence on Mitf. *Front Neuroanat* **9**, 149-149 (2015).
24. S. S. Joshi *et al.*, CD34 defines melanocyte stem cell subpopulations with distinct regenerative properties. *PLOS Genetics* **15**, e1008034 (2019).

25. L. Zecca *et al.*, Interaction of Human Substantia Nigra Neuromelanin with Lipids and Peptides. *Journal of Neurochemistry* **74**, 1758-1765 (2000).
26. L. Zecca *et al.*, Substantia nigra neuromelanin: structure, synthesis, and molecular behaviour. *Mol Pathol* **54**, 414-418 (2001).
27. R. L. Haining, C. Achat-Mendes, Neuromelanin, one of the most overlooked molecules in modern medicine, is not a spectator. *Neural Regen Res* **12**, 372-375 (2017).
28. D. Sulzer *et al.*, Neuromelanin detection by magnetic resonance imaging (MRI) and its promise as a biomarker for Parkinson's disease. *NPJ Parkinsons Dis* **4**, 11-11 (2018).
29. E. Vosoughi *et al.*, Survival and clinical outcomes of patients with melanoma brain metastasis in the era of checkpoint inhibitors and targeted therapies. *BMC Cancer* **18**, 490 (2018).
30. A. L. Antaris *et al.*, A small-molecule dye for NIR-II imaging. *Nature Materials* **15**, 235-242 (2016).
31. G. Hong *et al.*, Through-skull fluorescence imaging of the brain in a new near-infrared window. *Nat Photonics* **8**, 723-730 (2014).
32. Y. Zhong *et al.*, Boosting the down-shifting luminescence of rare-earth nanocrystals for biological imaging beyond 1500 nm. *Nat Commun* **8**, 737 (2017).

SI Appendix

Section S1 – Reported NIR-II fluorophores for transcranial brain imaging and its recent advances

Table S1. Recent advances in NIR-II fluorophores for transcranial brain imaging. An updated list of some of the most relevant NIR-II nanoprobes and their *in vivo* applications. (Wt = wild type, MCAO = Middle cerebral artery occlusion)

NIR fluorescent probe	Application	Animal model	$\lambda_{\text{emission}}$ (nm)	Reference
PbS (1100QDs)	Non-invasive imaging of brain vasculature during cerebral thrombosis	Lipopolysaccharide-neuroinflammation Hos:HR1 mouse	1100	(1)
Gd-Ag ₂ S QDs	Brain tumour resection assisted-surgery	Brain tumour U87MG nude mouse	1200	(2)
SWNT-IRdye800	Non-invasive through-skull fluorescence imaging of brain vasculature during ischemia	MCAO model C57BL/6J mouse	1300 - 1400	(3)
IR-E1	Non-invasive through-skull fluorescence imaging of brain hypo perfusion	Traumatic brain injury C57BL/6J mouse	1070	(4)
Er-RENPs	Non-invasive through-skull fluorescence imaging of brain vasculature	C57BL/6J mouse	1500	(5)
CH1055	Brain photoacoustic image guided brain tumour surgery	Brain tumour U87MG Nude mouse	1055	(6)
p-FE-CNTs	3D Confocal ultrafast imaging of brain blood flow	C57BL/6J mouse	1100 -1500	(7)
NaYF ₄ :Gd/Yb/Er	Non-invasive <i>in vivo</i> cerebral vascular imaging	Kunming mouse	1500- 1700	(8)
IR-BEMC6P organic dye	Brain tumour delineation during resection assisted-surgery	Brain tumour U87MG Nude mouse	1025	(9)
InAs CS. And CSS QDs	Invasive through-skull fluorescence imaging of brain blood flow and glioblastoma	Brain tumour with GL261 cells-GFP-GLUC	900 – 1600	(10)

ICG@Ag ₂ S	Non-invasive through-skull fluorescence imaging of brain vasculature and tumour.	Brain tumour Balb/c and Nude mouse	1100	(11)
Ag ₂ S			1060	
CH1000			990	
TB1			975	
TBI dots	Dual NIR-II fluorescence and photoacoustic non-invasive imaging of brain vasculature and tumour	Nude mouse	1156	(12)
FD-1080 dye	Non-invasive through-skull fluorescence imaging of brain vasculature and tumour.	Nude mouse	1080	(13)
CH1055	Non-invasive through-skull fluorescence imaging of brain vasculature and brain tumour imaging	C57BL/6J mouse Nude mouse Brain tumour U87MG	1055	(14)
CQS1000 dye	Non-invasive through-skull fluorescence imaging of brain	Wild-type healthy C57BL/6J mouse	1000	(15)
InAsCsDSe-CdS CSS- QDs	Non-invasive through-skull fluorescence imaging of brain vasculature	C57BL/6J mouse	1200	(16)
p-FE PbS/CdS QS	Non-invasive through-skull fluorescence imaging of brain	C57BL/6J mouse	850-1000 1500-1700	(17)
SWNTs-LV	Non-invasive through-skull fluorescence imaging of brain vasculature	Wt C57BL/6J mouse	1500-1700	(18)
IR-820	Non-invasive through-skull fluorescence imaging of brain vasculature during ischemia	MCAO model ICR mouse	700- 1300	(19)
IR-783@BSA	Non-invasive through-skull fluorescence imaging of brain vasculature	Wt C57BL6/J	1200	(20)

Table S1. Recent advances in NIR-II fluorophores for transcranial brain imaging. List of some of the NIR nanoprobes and their *in vivo* brain imaging applications. (Wt = wild type, MCAO = Middle cerebral artery occlusion).

Section S2 – Experimental setup for hyperspectral imaging

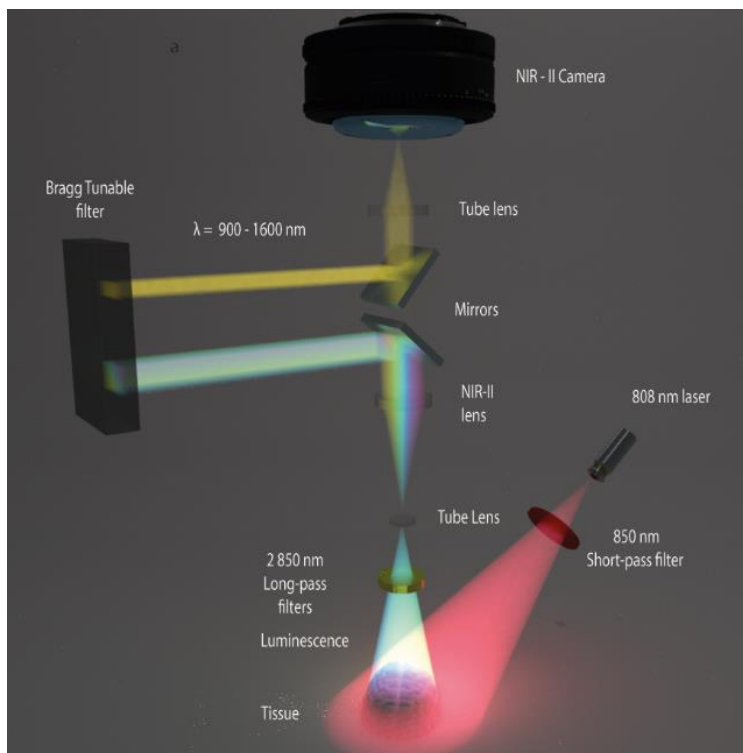


Figure S1. Hyperspectral Imaging. (a) Schematic representation of the hyperspectral imaging system used in this work.

Section S3 – Transmission and autofluorescence of the skull

To explain the darker region of **Figure 1C**, one needs to consider the different optical effects induced by the presence of the skull. According to previous works (21) the skull has an average transmittance of approximately 85% at 808 nm. As the skull is acting as an intermediate layer between the light source and the brain, only 85% of the brain autofluorescence gets to be emitted. Nevertheless, this emitted light also needs to pass through the skull. To quantify the amount of light originated at the brain that is detected after passing through the skull, one would also need to consider the transmittance spectrum of the skull in the proper wavelength range (22). One would also have to consider the transmittance of the skull, $T(\lambda)$, in the proper wavelength range.

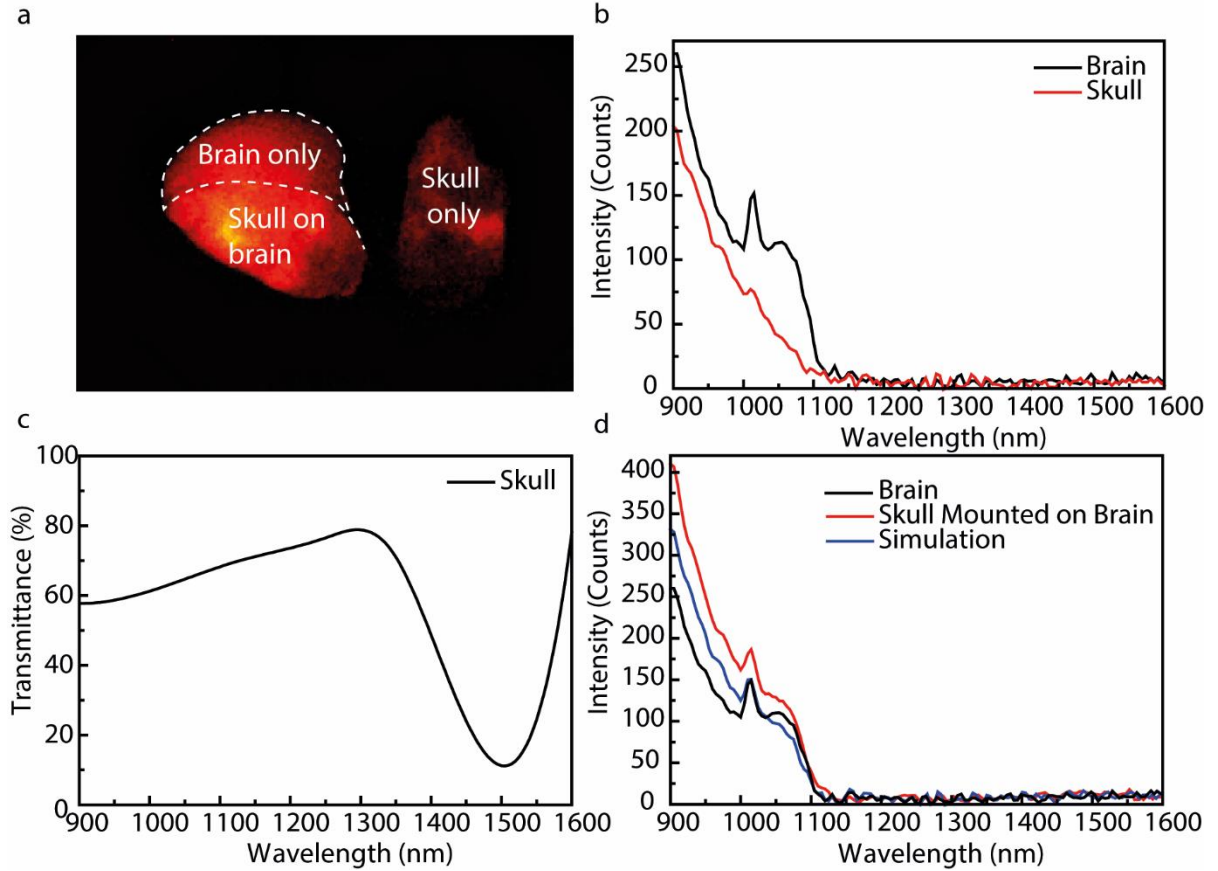


Figure S2. Optical effects induced by the skull. (a) Narrowband fluorescence image of a brain half covered by a piece of skull (left) and a piece of skull isolated (right). (b) Comparison of autofluorescence spectra of the isolated brain and skull. (c) Transmittance of the skull in the 900-1600 nm wavelength range according to previously published data (22). (d) Comparison between the autofluorescence provided by the isolated brain (black), the skull mounted on the brain (red) and the simulation using the data of (22) for the values of transmittance.

Additionally, as experiments confirm (see **Figs. S2A and B**), when the skull is excited at 808 nm, it presents an autofluorescence, $I_{\text{skull}}(\lambda)$, characterized, by a tail in the 900-1600 nm range with an intensity that is about half of that presented by brain tissues alone under the same conditions.

The combination of light attenuation and intrinsic autofluorescence of the skull, therefore, determines that, at a given wavelength, λ , the detected light will be approximately given by:

$$I_{skull+brain}^{det}(\lambda) = 0.8 \cdot I_{brain}^{uncov}(\lambda) \cdot T_{skull}(\lambda) + I_{skull}(\lambda) \quad (\text{Eq. S1})$$

where $I_{brain}^{uncov}(\lambda)$ is the autofluorescence of the brain when it is not covered by any tissue.

By measuring the autofluorescence spectra of an isolated brain and an isolated skull and using published data on the transmission of NIR light in the skull (**Figure S2C**), we have estimated the relationship between the signal obtained from the skull + brain structure and the one that comes from the isolated brain (**Figure S2D**). We have observed that the skull increases the absolute intensity of the fluorescence in the 900-1600 nm range. This is also observed in the *ex vivo* autofluorescence spectrum obtained with a brain + skull structure. Though differences in the absolute values of intensity exist between the simulation and experimental data (which, in turn, could attributed to factors such as the reflection of light on the brain-skull interface), their trend is the same: the presence of the skull increases the detected autofluorescence. Therefore, we can conclude that the darker region in **Figure 1C** is not an artifact but an indication of the contribution given by the skull.

Section S4 – Comparison with published data

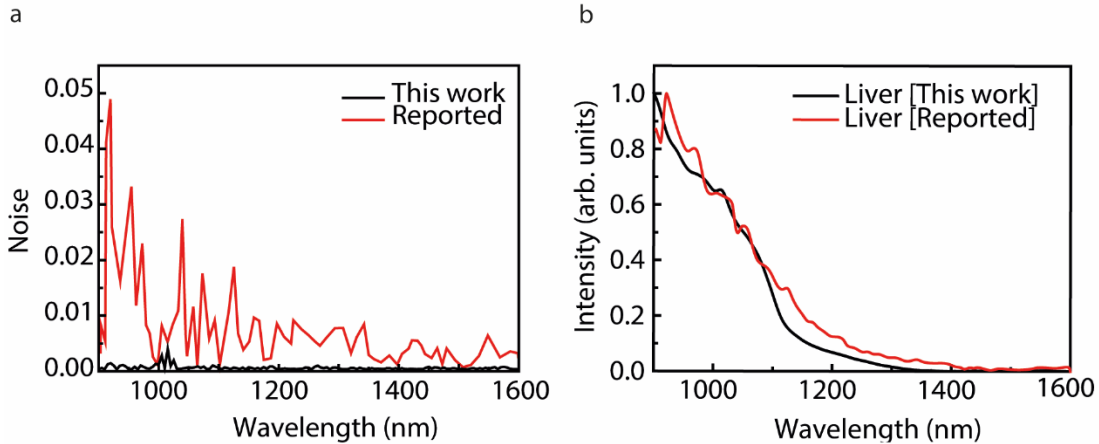


Figure S3. Residual spectra for reported NIR-II liver autofluorescence and the data obtained in this work. (a) Residual spectra was calculated for both reported and experimentally obtained curves after applying the Savitzky-Golay smoothing method (Polynomial order 5, 9 points of window). (b) Original spectra from which the noise was estimated (23).

Section S5 – Ratiometric imaging of several tissues

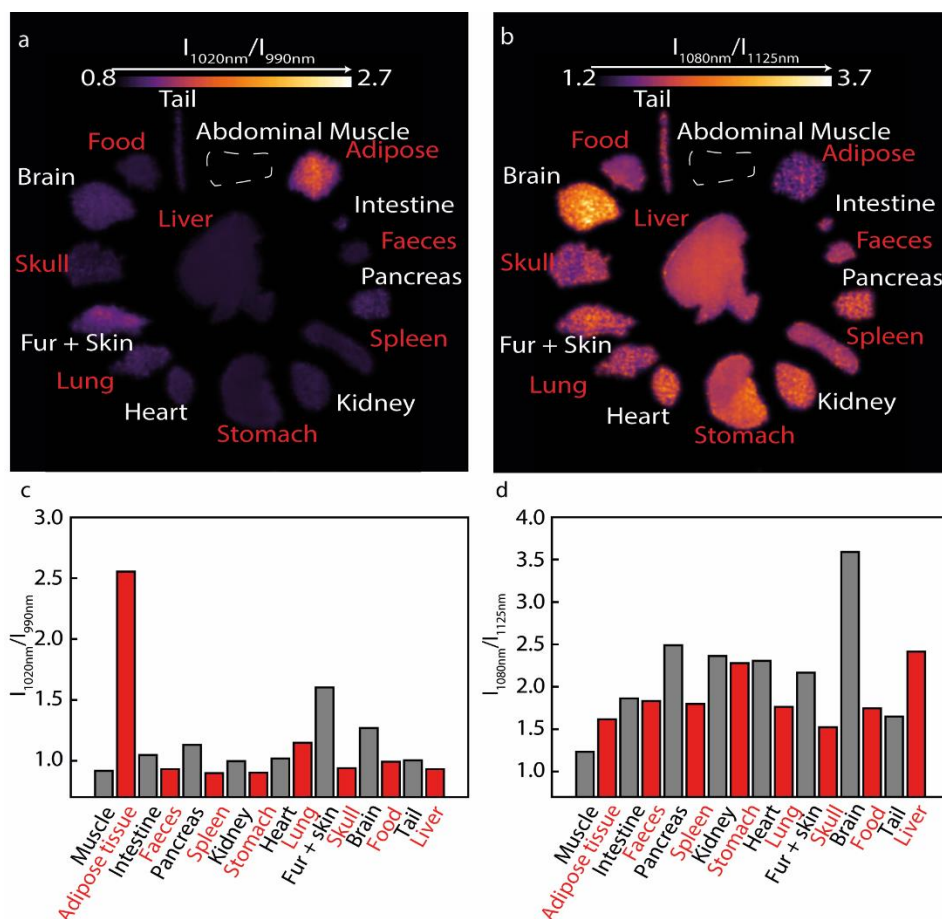


Figure S4. Ex vivo ratiometric images of different tissues and organs. Figure S III: Ratiometric images of the different tissues. (a) Ratiometric image as obtained by calculating the ratio between emitted intensities at 1080/1125 nm. **(b)** Ratiometric image as obtained by

calculating the ratio between emitted intensities at 1020/990 nm. **(c)** Intensity ratio between 1080 and 1125 nm. **(d)** Intensity ratio between 1020 and 990 nm.

Section S6 – Frontal view of a C57BL/6J mouse brain.

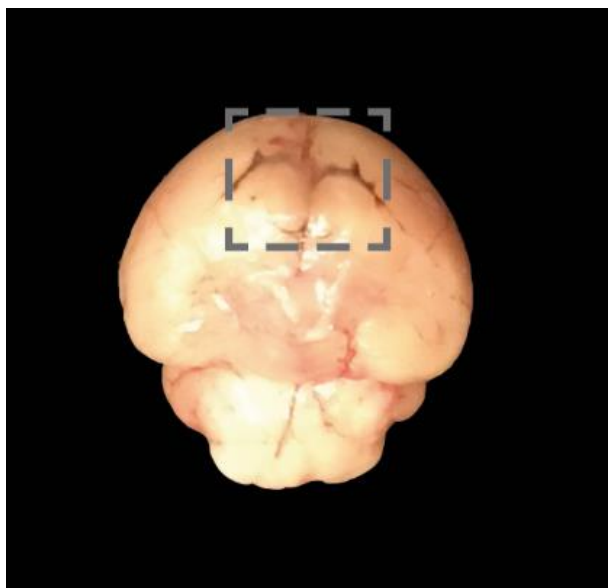


Figure S5. Optical Frontal view of the brain of a C57BL/6J mouse. The olfactory bulb has been removed to expose the frontal area in which meningeal melanocytes enriched in neuromelanin can be observed by naked-eye examination (grey square).

Section S7 – References

1. Y. Imamura *et al.*, Near-Infrared Emitting PbS Quantum Dots for in Vivo Fluorescence Imaging of the Thrombotic State in Septic Mouse Brain. *Molecules* **21**, 1080 (2016).
2. C. Li *et al.*, Preoperative Detection and Intraoperative Visualization of Brain Tumors for More Precise Surgery: A New Dual-Modality MRI and NIR Nanoprobe. *Small* **11**, 4517-4525 (2015).
3. G. Hong *et al.*, Through-skull fluorescence imaging of the brain in a new near-infrared window. *Nat Photonics* **8**, 723-730 (2014).
4. X.-D. Zhang *et al.*, Traumatic Brain Injury Imaging in the Second Near-Infrared Window with a Molecular Fluorophore. *Advanced Materials* **28**, 6872-6879 (2016).
5. Y. Zhong *et al.*, Boosting the down-shifting luminescence of rare-earth nanocrystals for biological imaging beyond 1500 nm. *Nat Commun* **8**, 737 (2017).

6. S. Kurbegovic *et al.*, Molecular Targeted NIR-II Probe for Image-Guided Brain Tumor Surgery. *Bioconjugate Chemistry* **29**, 3833-3840 (2018).
7. H. Wan *et al.*, A bright organic NIR-II nanofluorophore for three-dimensional imaging into biological tissues. *Nat Commun* **9**, 1171-1171 (2018).
8. Z. Xue, S. Zeng, J. Hao, Non-invasive through-skull brain vascular imaging and small tumor diagnosis based on NIR-II emissive lanthanide nanoprobe beyond 1500 nm. *Biomaterials* **171**, 153-163 (2018).
9. R. Tian *et al.*, Rational design of a super-contrast NIR-II fluorophore affords high-performance NIR-II molecular imaging guided microsurgery. *Chem Sci* **10**, 326-332 (2018).
10. O. T. Bruns *et al.*, Next-generation in vivo optical imaging with short-wave infrared quantum dots. *Nature Biomedical Engineering* **1**, 0056 (2017).
11. B. Guo *et al.*, Precise Deciphering of Brain Vasculatures and Microscopic Tumors with Dual NIR-II Fluorescence and Photoacoustic Imaging. *Advanced Materials* **31**, 1902504 (2019).
12. W. Yu *et al.*, NIR-II fluorescence in vivo confocal microscopy with aggregation-induced emission dots. *Science Bulletin* **64**, 410-416 (2019).
13. B. Li, L. Lu, M. Zhao, Z. Lei, F. Zhang, An Efficient 1064 nm NIR-II Excitation Fluorescent Molecular Dye for Deep-Tissue High-Resolution Dynamic Bioimaging. *Angewandte Chemie International Edition* **57**, 7483-7487 (2018).
14. A. L. Antaris *et al.*, A small-molecule dye for NIR-II imaging. *Nature Materials* **15**, 235-242 (2016).
15. K. Shou *et al.*, Multifunctional Biomedical Imaging in Physiological and Pathological Conditions Using a NIR-II Probe. *Advanced Functional Materials* **27**, 1700995 (2017).
16. D. Franke *et al.*, Continuous injection synthesis of indium arsenide quantum dots emissive in the short-wavelength infrared. *Nat Commun* **7**, 12749 (2016).
17. F. Wang *et al.*, Optical Sectioning of Live Mammal with Near-Infrared Light Sheet. *bioRxiv* 10.1101/447433, 447433 (2018).
18. S. Diao *et al.*, Fluorescence Imaging In Vivo at Wavelengths beyond 1500 nm. *Angewandte Chemie International Edition* **54**, 14758-14762 (2015).
19. Z. Feng *et al.*, Excretable IR-820 for in vivo NIR-II fluorescence cerebrovascular imaging and photothermal therapy of subcutaneous tumor. *Theranostics* **9**, 5706-5719 (2019).
20. R. Tian *et al.*, Albumin-chaperoned cyanine dye yields superbright NIR-II fluorophore with enhanced pharmacokinetics. *Science Advances* **5**, eaaw0672 (2019).
21. N. Davoodzadeh *et al.*, Theranostic cranial implant for hyperspectral light delivery and microcirculation imaging without scalp removal. *bioRxiv*, 720599 (2019).
22. M. S. Cano-Velázquez *et al.*, Enhanced near infrared optical access to the brain with a transparent cranial implant and scalp optical clearing. *Biomed. Opt. Express* **10**, 3369-3379 (2019).
23. S. Diao *et al.*, Biological imaging without autofluorescence in the second near-infrared region. *Nano Research* **8**, 3027-3034 (2015).